RESEARCH PAPER

On the use of gas-metal-arc-welding additive manufacturing for repurposing of low-carbon steel components: microstructures and mechanical properties

Van Thao Le [1,2] · Henri Paris [3]

Abstract

In this paper, the utilization of gas-metal-arc-welding additive manufacturing (GMAWAM) for the repurposing of components was explored. Herein, the GMAWAM process was used to build new low-carbon steel features on an existing low-carbon steel component to obtain a new part with new functionalities. To confirm the internal quality of the new part obtained by such a strategy that is adequate for real applications, its material properties were investigated. The obtained results reveal that the new features (i.e., thin walls) built by GMAWAM possess different microstructure types. The upper region of thin-walled features exhibits lamellar structures, whereas the middle region is characterized by granular structures, and mixed equiaxed and lamellar grains appear in the bottom region. Particularly, the new features have an excellent bonding strength with the existing part. The material properties of GMAWAM-repurposed parts also meet industrial requirements, confirming that the GMAWAM-repurposed parts are adequate with real applications.

1 Introduction

Additive manufacturing (AM) technologies are receiving much attention from both the industrial and academic fields because of their capability of manufacturing complex geometries including internal structures and parts made of hardly machined materials. Based on the layer-by-layer manufacturing principle, AM uses only an amount of materials that is needed to build the designed parts plus an allowance necessary for finishing operations and support structures if necessary. Therefore, material wastes and environmental impacts

can be reduced [1, 2]. Moreover, through the topological optimization in designing a lightweight part that AM is capable of fabricating, raw materials can be saved [3]. AM is nowadays applied successfully in aerospace, automotive, and biomedical engineering [4].

According to the classification in [5], there are three main groups of metal-based AM systems: powder bed fusion (PBF), powder feed deposition (PFD), and wire feed deposition (WFD) systems. PBF-AM systems use a high-power laser source or electron beam as a heat source to melt metal powder in a powder bed layer-by-layer. On the other hand, PFD-AM systems use a deposition head or a powder nozzle to jet metal powder with the shielding gas into the work area and build the designed part layer-by-layer. The metal powder can be melted by laser or electron beam. In WFD-AM systems, the feedstock is the metal wire and the head source can be electron beam, laser beam, and arc welding. Among WFD-AM systems, wire arc additive manufacturing (WAAM) is the most popular technology.

The main advantages of PBF-AM systems are the possibility of building very complex parts, including internal structures. However, these systems are only suitable to build components with small and medium sizes due to their limited building volume. It is also difficult or impossible to use these

✉ Van Thao Le
thaomta@gmail.com

1 Institute of Research and Development, Duy Tan University, Da Nang 550000, Vietnam

2 Advanced Technology Center, Le Quy Don Technical University, Hanoi, Vietnam

3 CNRS, Grenoble INP, G-SCOP, Univ. Grenoble Alpes, F-38000 Grenoble, France

systems for repairing, remanufacturing, and repurposing applications [6]. On the other hand, PFD-AM systems are more suited for the manufacture of larger parts and repairing/remanufacturing applications, because they use a large and flexible configuration of 5-axis machine tools or robots [6]. In comparison with BPF-AM and PFD-AM systems, WAAM reveals a number of remarkable advantages, such as high material deposition rate, high energy efficiency [7], and significantly low costs of equipment investment [8]. The deposition rate of WAAM can reach up to 10 kg/h, whereas that of PBF-AM and PFD-AM is about 0.1–0.2 kg/h and 2.27 kg/h, respectively [9]. The components of WAAM machines can also be ordered from many suppliers in the welding industry [10]. Moreover, using wire as feedstock is more efficient in the usage of the input material (up to 99% of the wire material is deposited into parts), is safer for the operators' health, and can reduce environmental impacts. Lastly, the price of the metal wire is significantly lower than that of the metal powder used in powder-based AM technologies [11].

In WAAM, the heat source can be GMAW (gas metal arc welding), GTAW (gas tungsten arc welding), and PAW (plasma arc welding) [12]. In PAWAM and GTAWAM processes, the plasma arc and the electrical arc are generated between a tungsten electrode and the part/substrate, and melted material is fed into the molten pool. On the other hand, in the gas-metal-arc-welding additive manufacturing (GMAWAM) process, the electrical arc is directly generated between the consumable electrode (i.e., metal wire) and the part/substrate. Thus, the wire is melted and fed more quickly into the welding pool. The rate of material deposition in GMAWAM is two or three times higher than that in GTAWAM and PAWAM [13]. For example, in the case of depositing AISI 316L stainless steel, the deposition rate of GMAWAM, PAWAM, and GTAWAM (with suitable quality) can reach up to 5 kg/h, 3.5 kg/h, and 1.5 kg/h, respectively [14]. Hence, the GMAWAM process is more suited to build components with large dimensions.

Many studies have explored the effects of processing parameters and thermal cycles in WAAM on the shape and dimensional accuracy of built components [12, 15–17]. For instance, Xiong et al. [12] reported the influence of interlayer temperature, traveling speed, and wire feed speed on the surface appearance of GMAWAM thin-walled components. These authors stated that the surface quality could be enhanced by increasing the traveling speed. The decrease of the interlayer temperature could also increase the surface quality of thin-walled components. Zhao et al. [18] demonstrated that residual stresses could be reduced by increasing the idle time between two adjacent layers. However, if more idle time is applied, the productivity will be decreased. Suryakumar et al. [19] highlighted that the thermal cycle of the current layer (called the ith layer) in WAAM had slight effects on the $(i$-5)th layer. The top layer of WAAM-built parts also

presented the highest hardness value. Liberini et al. [20] reported the effect of voltage and traveling speed on microstructures and microhardness of GMAWAM low-carbon steel components. These authors found that there is no substantial difference in terms of microstructures of thin-walled samples, which were built with different levels of voltage and traveling speed. However, the tensile properties of GMAWAM components were not yet investigated. Recently, Rafieazad et al. [21] also explored the microstructure and mechanical properties of multi-layer multi-bead low-carbon steel parts fabricated by using a WAAM process. These authors reported that the tensile strengths of the specimens extracted in the building direction and the welding direction were comparable.

Although much research has been realized on the GMAWAM process, no study has reported on the utilization of GMAWAM for repurposing applications. Repurposing is a strategy of reusing end-of-life components, which aims to preserve the added value of used components by reusing them in new applications [23]. To fill this gap, this paper aims at demonstrating the feasibility of using GMAWAM in a repurposing context. Herein, the proposed repurposing strategy aims at reusing the material of an end-of-life component directly to produce a new part without passing through the recycling stage of materials [1, 24, 25] by using the combination of GMAWAM and CNC machining processes, as illustrated in Fig. 1. Using such a strategy, not only the added value of end-of-life components can be preserved but also environmental impacts and manufacturing costs can be reduced [1]. In this context, all materials become interesting. For low-carbon steels, many end-of-life components such as broken/damaged rotating shafts can effectively be repurposed into new shafts for new applications.

In practice, the material properties of repurposed parts are considered one of the most important criteria that need to be
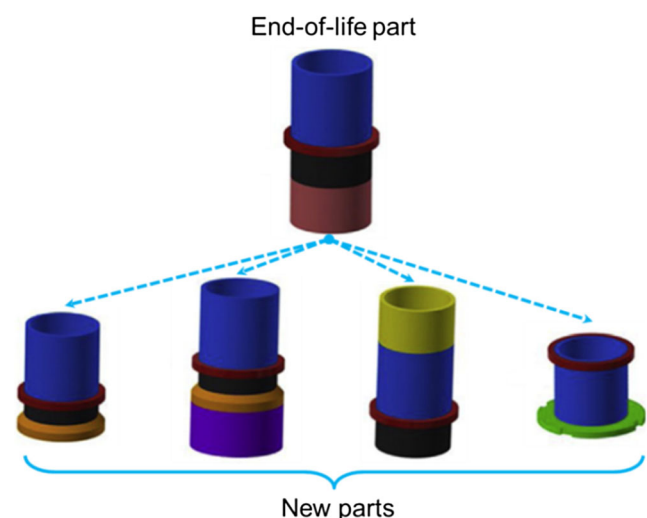

Fig. 1 Illustration of the repurposing strategy, in which the material of an end-of-life part is reused directly to produce new parts (adapted from [22])

evaluated for the decision-making. Hence, the current study focuses on analyzing the material properties of GMAWAM-repurposed parts. For this purpose, new thin-walled features were built on the plates, which are considered the existing/used components by using the GMAWAM process, as depicted in Fig. 2. The material properties of new parts, including new features and the reused part, were investigated. The bonding strength between new features and the material base of existing components was also analyzed. This allows us to verify the "material health" of repurposed parts for real applications.

2 Experimental methods

In this work, two low-carbon steel plates (SS400) were used as existing components to build the test samples. Their dimensions are 250 mm × 120 mm × 20 mm (length × width × thickness). The copper-coated low-carbon steel wire (ER70S-6) was used to build new features (i.e., thin walls) on the substrates. The diameter of welding wire is 1.2 mm. The chemical composition of the ER70S-6 wire and the SS400 substrate is presented in Table 1.

The GMAWAM system is presented in Fig. 3a. This system uses an industrial 6-axis robot Panasonic TA-1400 (1) to execute the movement of the GMAW torch (4) during the deposition of materials on the substrates (Fig. 3b). The robot controller (2) controls the robot's motions, whereas the welding process parameters are controlled by the welding power source (3).

To build new thin-walled features on the plates, a set of processing parameters, including a traveling speed of the welding torch of 300 mm/min, a welding current of 90 A, and a voltage of 18 V were used. Before the deposition of welding layers, the surface of the plates was ground to remove oxide scale and contaminate. The method for building the thin-walled features was illustrated in Fig. 3b. The welding paths were depicted by the red lines and the paths without welding are the green lines. An idle time (T_{id}) of 60 s was also

applied between two adjacent deposits to cool down the built feature by the atmosphere. The value of the idle time was chosen according to the previous studies [20, 28]. Subsequently, the next deposit was performed upon the previous one in the opposite direction (Fig. 3b). Moreover, the CO_2 gas was employed for the shielding purpose during the welding process. The flow rate of the shielding gas is fixed at 16 L/min. No preheating of the substrate was used in the experiment.

In this work, a new thin-walled feature (denoted by TWF1) was built on the first plate to investigate the microstructure and hardness of materials. The second plate was used to build another thin-walled feature (denoted by TWF2) for preparing the tensile test specimens. The dimensions of TWF1 are 80 mm × 32 mm × 4.5 mm (length × height × thickness), and those of TWF2 are about 200 mm × 80 mm × 4.5 mm (length × height × thickness).

To investigate the microstructure and hardness of repurposed parts, a specimen including the welded material (i.e., a part of thin-walled feature) and the base material (i.e., a part of the substrate) (Fig. 4) was cut from the TWF1 and the substrate in the middle region by using a wire-cut EDM machine. The cross-sectional surface of this specimen was subsequently polished and chemically etched by using an etching solution of 5% Nital. Then, a microscope AXIO imager A2M of Carl Zeiss was employed to analyze the microstructure in 5 regions: the upper region, the middle region, the bottom region of the thin-walled feature, the intersecting region between the new feature and the substrate, and the substrate region (Fig. 4).

The hardness (HV5) was measured in five regions of the specimen (Fig. 4) by using a digital Vickers Hardness Tester of Wolpert Wilson Instruments. An idle time of 10 s and a load of 49.05 N were applied in each hardness test. The measurement of hardness was performed at 5 positions in the upper, the bottom, the intersecting region, and the substrate region, and at 7 positions in the middle region. The measured positions were distributed on the centerline of the cross section (dashed yellow line in Fig. 4).

Fig. 2 Illustration of the existing part (a) and the repurposed part with a new thin-walled feature (b)
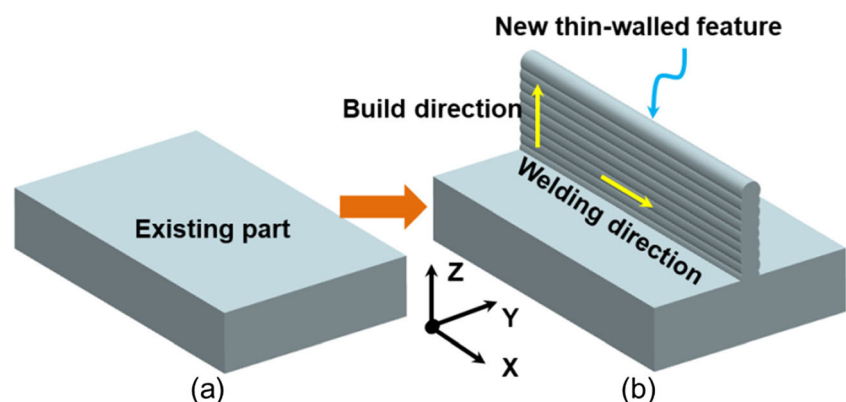
Table 1 Chemical composition of the wire and the substrate (in wt.%)

Element	C	Mn	Si	S	P	Cr	Ni	Mo	V	Cu	Fe
The ER70S-6 wire [26]	0.06–0.15	1.40–1.85	0.80–1.15	0.035 max	0.025 max	0.15 max	0.15 max	0.15 max	0.03 max	0.50 max	Bal.
The SS400 substrate [27]	0.05	0.46	0.037	0.002	0.013	-	-	-	-	-	Bal.

To prepare the tensile specimens, two side surfaces of the TWF2 were machined to achieve the effective width of the deposited material. Subsequently, three groups of tensile specimens were extracted from the TWF2 and the substrate by using the same wire-cut EDM machine (Fig. 5a). Three vertical tensile specimens in the building direction Z (v-TS1, v-TS2, and v-TS3) and three horizontal tensile specimens in the welding direction X (h-TS1, h-TS2, and h-TS3) were cut from the left and right sides of the machined TWF2 in the XZ plane (Fig. 5a). Their dimensions were chosen according to the international standard (ASTM A370), as shown in Fig. 5b. These specimens were used to analyze the tensile properties of the built thin-walled feature in both the building direction and the welding direction.

Three tensile specimens (b-TS1, b-TS2, and b-TS3) for evaluating the bonding strengths between the built features and the plate were cut in the middle region. They are composed of a part of the deposited material and a part of the base material, as shown in Fig. 5a. The top portion of these specimens is identical to a half of a specimen v-TSi or h-TSi (where i = 1, 2, and 3). Their dimensions are given in Fig. 5c.

The tensile tester (INSTRON 3369) was used to implement the tensile tests. Figure 5d and e present the installation of the

specimens (v-TSi/h-TSi) and the specimens (b-TSi) on the tensile tester, respectively. The tensile tests were performed at room temperature and in the vertical direction. The cross-head displacement speed is 1.2 mm/min.

3 Results and discussion

3.1 Microstructure analysis

From the microscopy images, it is firstly found that the specimen did not show any major defect (e.g., cracks and macroporosity) in both the thin-walled feature and the interface region between the new feature and the existing part. The fusion of material in adjacent layers was excellent.

In the build of single-bead multi-layer parts by using the WAAM process, except for the last layer, the fore layers were reheated and partially re-melted by the heat input that formed the rear layers, causing different thermal cycles in different regions [29]. In the free-cooling condition (i.e., the built parts were cooled down by the atmosphere of the experiment room), the heat accumulation also increases with the deposited height. Consequently, the cooling time becomes longer in higher layers [30]. Therefore, the new thin-walled feature built by GMAWAM reveals different microstructures in different regions (i.e., the upper region, the middle region, and the bottom region).

The upper region consists of the last deposited layer. The microstructure of the upper region is characterized by lamellar structures consisting of ferrites with different morphologies—
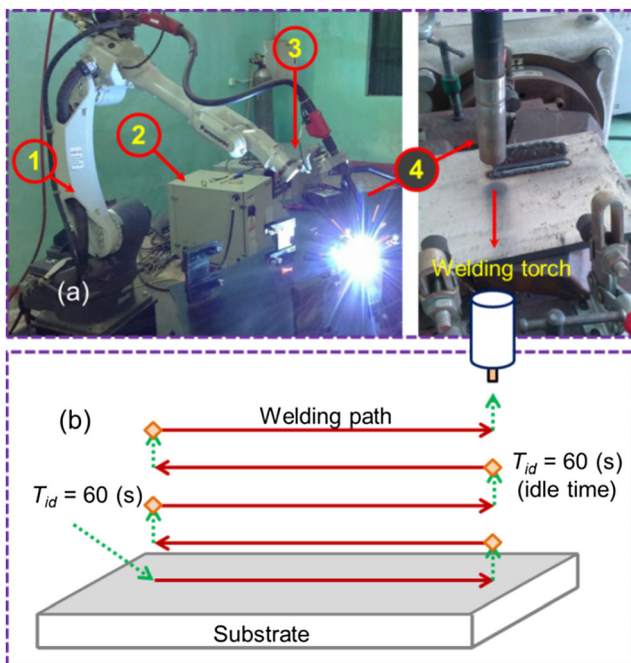

Fig. 3 The GMAWAM system (a) and the strategy for building new thin-walled features (b)
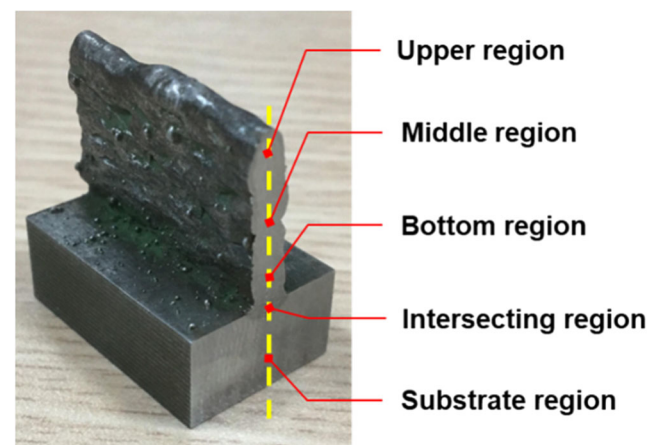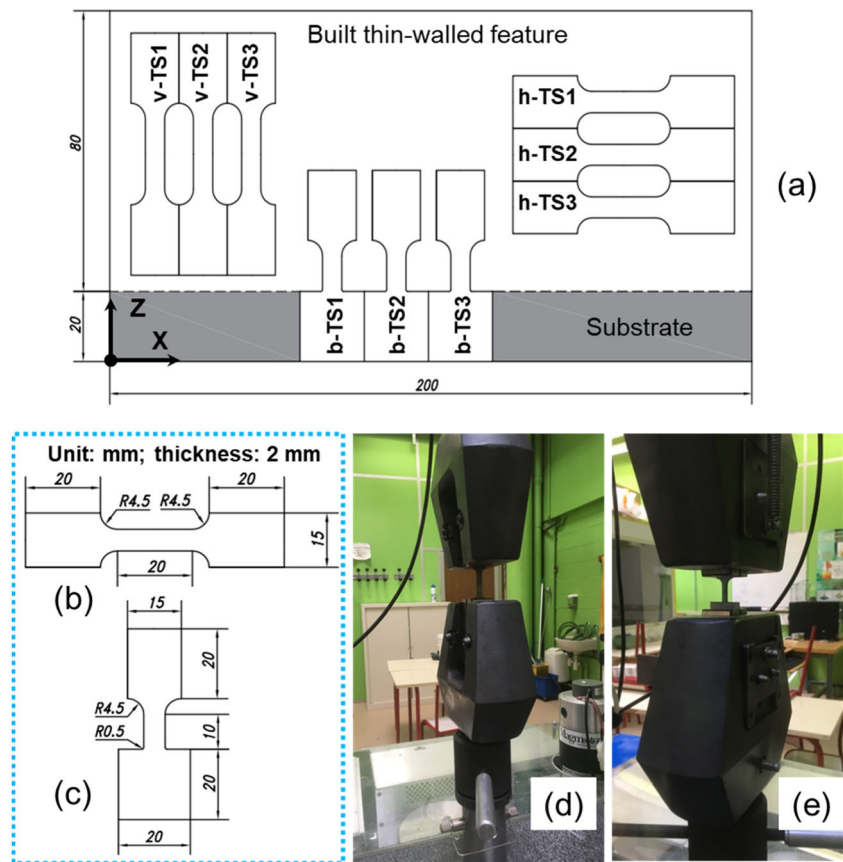

**Fig. 4** Specimen for investigating the microstructure and hardness

Fig. 5 a Illustration of the positions for cutting tensile specimens from the TWF2 and the substrate, the dimensions of the tensile specimens {v-TS*i*, h-TS*i*} (b) and the specimens {b-TS*i*} (c), and the installation of the specimens v-TS*i*/h-TS*i* (d) and b-TS*i* (e) on the tensile test machine (where *i* = 1, 2, and 3)

allotriomorphic ferrite (α), acicular ferrite (α_a), and Widmanstätten ferrite (α_w), as shown in Fig. 6a. Indeed, the upper region (i.e., the last layer) did not undergo the thermal effect of other layers. The upper region only contacted the warm surface of the fore layer and the air at room temperature. Consequently, there is a transformation of primary austenite dendrites into allotriomorphic ferrite (α), acicular ferrite (α_a), and Widmanstätten ferrite (α_w) structures. This type of micro-structures is similar to that reported in previous studies [21, 31, 32]. Moreover, a transition of microstructures from the lamella to granular structures was also observed in the lowest location of this region (Fig. 6b). It reveals a mix microstructure, including lamellar and equiaxed microstructures.

The middle region mainly reveals granular structures composed of ferrite grains and a small amount of pearlite, which appears in the boundaries of ferrite grains (Fig. 7). Moreover, it is also found two types of microstructures in this region: the finer granular grains were observed in the center of the molten pool of a deposited layer (region (1), Fig. 7b), and the larger granular grains were generated in the heat-affected zone (2) between two successive layers (Fig. 7c). The average grain size in the heat-affected region is 13.60 ± 5.64 μm, whereas that in the center of the molten pool (1) is 5.50 ± 1.76 μm. The reason is that the previous layer (i-1) was reheated and partial-ly re-melted by the heat of the molten pool of the deposit (i). This results in coarser grains in the heat-affected zone (2)

Fig. 6 Microstructures in the upper region of thin-walled feature (**a**) and the transition of microstructures between the upper region and the middle region (**b**)
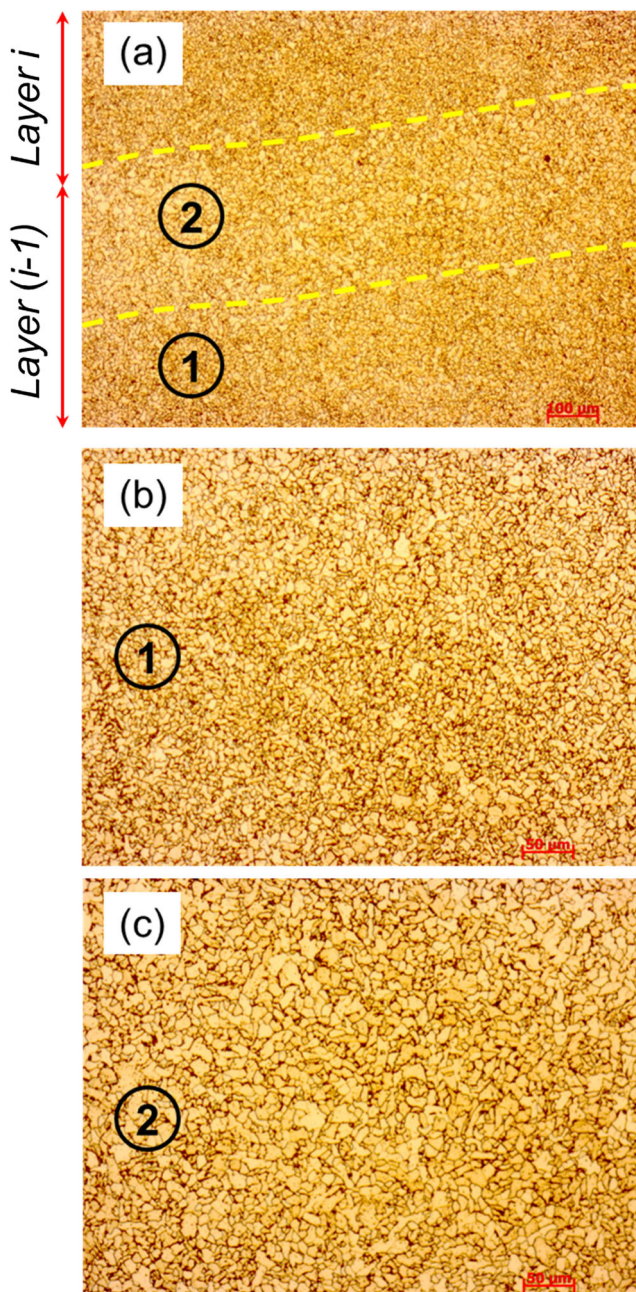
Fig. 8 Microstructure in the bottom region of the thin-walled feature
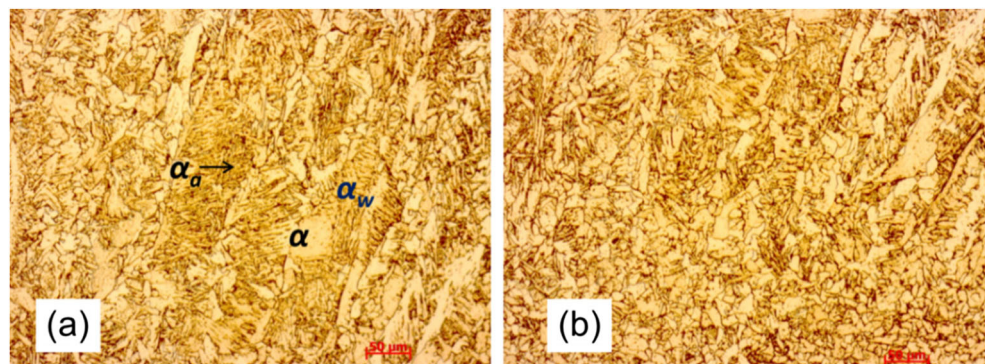
Fig. 7 Typical microstructure in the middle region of the new feature at a low magnification (**a**), the microstructures at a high magnification in the center (1) of a layer (**b**), and in the heat-affected zone (HAZ) (2) between two successive layers (**c**)

between two successive layers. The microstructure characterization of the middle region of the thin-walled feature is also similar to that observed in the middle region of multi-bead multi-layer low-carbon steel components fabricated by using GMAWAM [21, 32].

The bottom region is composed of a mix of equiaxed and lamellar/acicular structures, as shown in Fig. 8. It is also found that the ferrite coexists in equiaxed form with thin strips of pearlite. In addition, the bottom region reveals that the grain size is finer than that in the middle region. Indeed, the bottom region
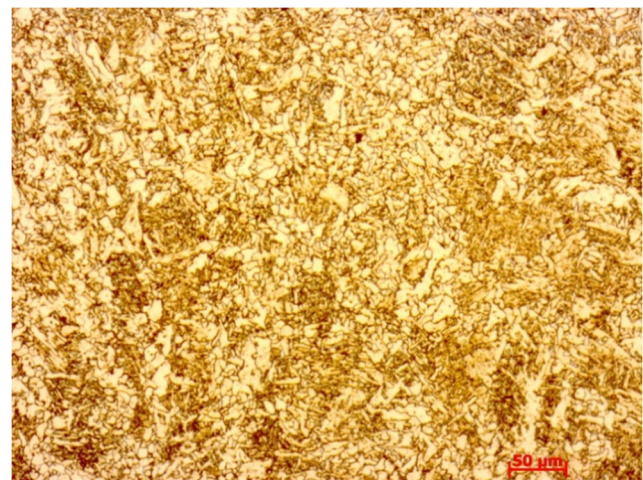
contacts the large substrate, which was assumed to be at room temperature. This leads to a higher thermal gradient and a higher cooling rate with respect to the middle region [30]. In the middle region, the heat accumulation increases with an augmentation in the number of deposits. At higher layers, the effective area for transferring the heat decreases, leading to the heat dissipation to also decrease. As a result, the cooling rate in the middle region must be lower than that in the bottom region.

Figure 9a exhibits an overall structure of the intersecting region between the new feature and the existing part. The microstructure in the fusion zone (FZ) of the first deposit (Fig. 9b) is similar to that in the bottom region (Fig. 8). The heat-affected zone (HAZ) of the base materials adjacent to the first welded layer was raised because of a high temperature of the first deposit. It is revealed that the microstructure varies according to the heat-affected depth and was limited by nearly parabolic boundaries (Fig. 9a). It can be found a transformation of microstructures from austenite in the FZ (Fig. 9b) to martensite in the coarse-grained HAZ (CGHAZ) (Fig. 9c), and the martensite is visible within the austenite grains. The main reason is that the CGHAZ was heated by the energy source of the first deposit, and subsequently rapidly cooled by the surrounding base metal. In the fine-grained HAZ (FGHAZ) (Fig. 9d), the proeutectoid ferrite and pearlite were refined in comparison with those of the substrate region (Fig. 10). The substrate region exhibits typical structures that are composed of ferrite bands and pearlite bands of the thick steel plate obtained by using a hot rolling process [33].

In summary, different microstructure types from the top of the built thin-walled features to the substrate were observed. The presence of complex thermal cycles during the deposition of successive layers is the main factor, which causes the microstructural non-uniformity along the height of built thin-walled features. The repurposed component also reveals a continuous microstructure transition in the intersecting region between the new feature and the existing part, indicating a good metallurgical bonding between the new built features and the base part.
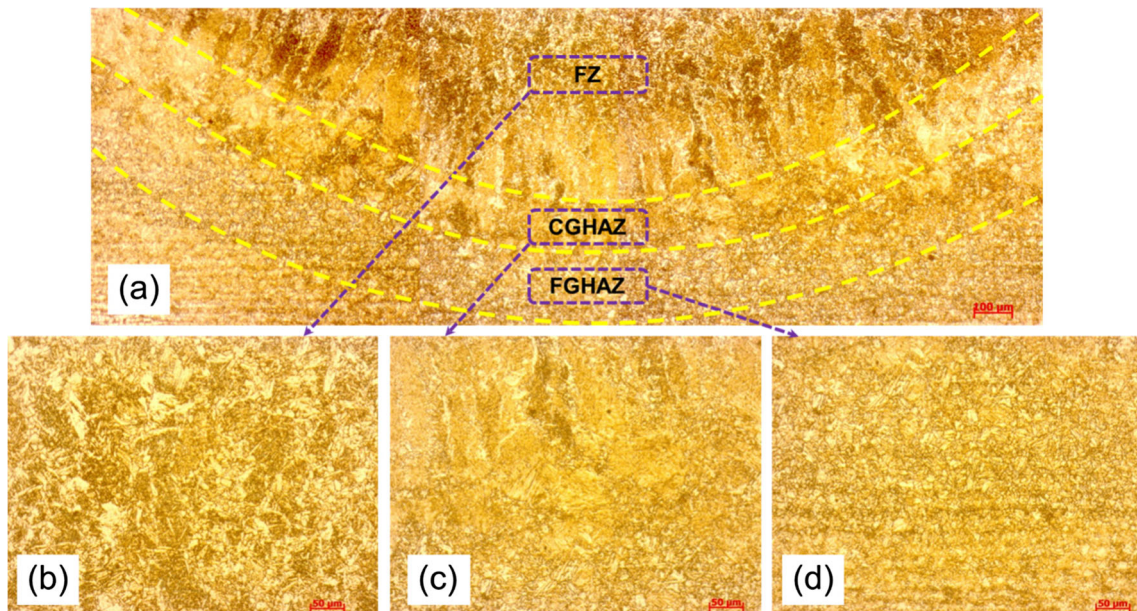
Fig. 9 Overall structure in the intersecting region at low magnification (a), the microstructure at a higher magnification in the fusion zone (FZ) of the first deposit (b), in the coarse-grained HAZ (CGHAZ) (c), and in the fine-grained HAZ (FGHAZ) (d)

3.2 Mechanical properties

Figure 11 presents the average hardness value of each region. In the new feature, the middle region is the softest with an average hardness value of 176 ± 2 HV, followed by the bottom region (195 ± 7 HV) and the top region (205 ± 5 HV). This result is coherent with microstructures of the specimen observed in Section 3.1. The upper region presents higher hardness values than those of other regions because of the presence of Widmanstätten lamellar structures (Fig. 6). Similarly, due to the presence of lamellae/acicular structures in the bottom region (Fig. 8), the average hardness value in this region is greater than that in the middle region. The average hardness value in the middle region is also comparable to that in the middle region of GMAWAM thin-walled low-carbon steel components published in previous studies [7, 21, 34]. The intersecting region shows an average hardness value of 245 ± 19 HV higher than that of the substrate region ($182 \text{ HV} \pm 3$ HV). In comparison with the hardness of GMAWAM multi-bead multi-layer components made of the same material (ER70S-6), the average hardness in each region of new features (i.e., single-bead multi-layer walls) is generally higher. For instance, the average hardness value of GMAWAM multi-bead multi-layer low-carbon steel (ER70S-6) components reported in [21] is 160 ± 7 HV, which is also relatively lower than that observed in this study. Lastly, the GMAWAM-built features have an average hardness value higher than the maximum value of 168 (HV) for wrought
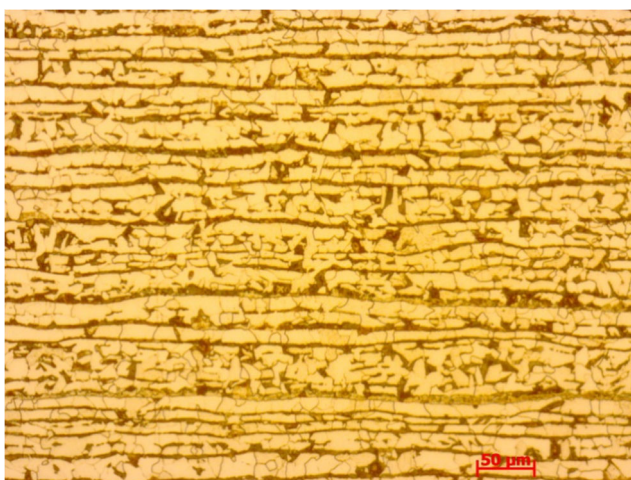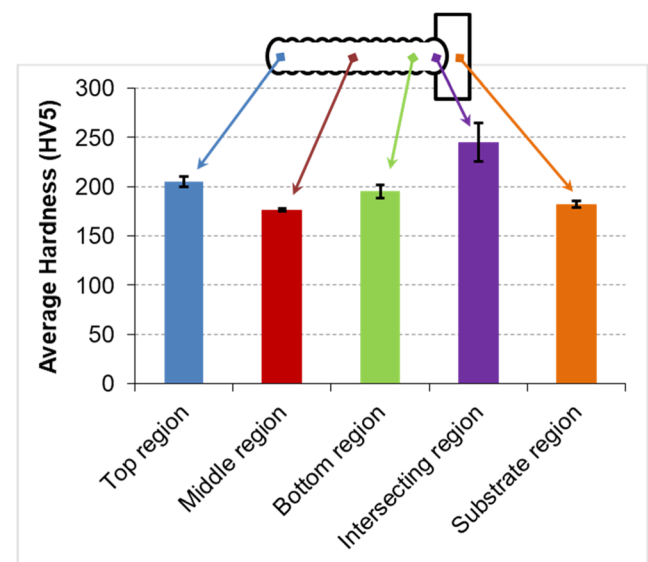

Fig. 10 Microstructure in the plate region

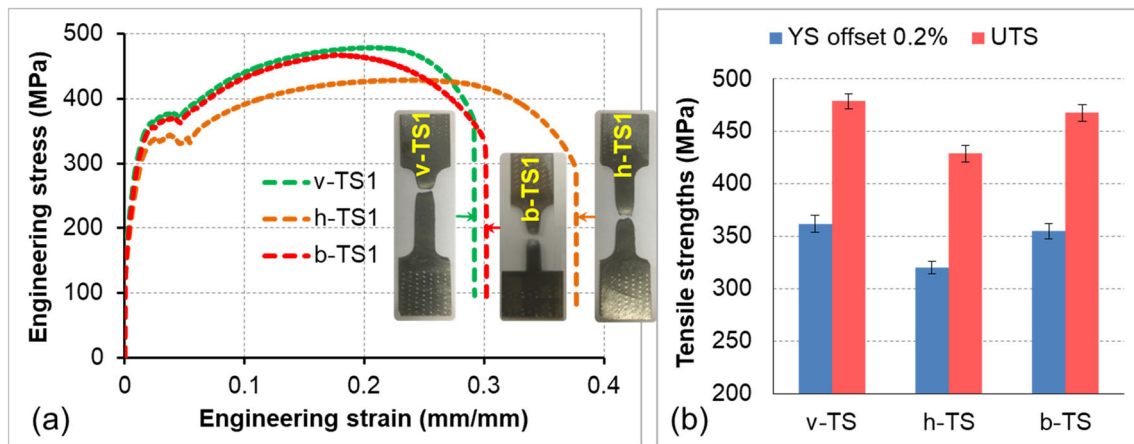**Fig. 11** Hardness values in different regions of the specimen

Fig. 12 Engineering stress-strain curves of three tensile specimens v-TS1, h-TS1, and b-TS1 (on the left), and the average value of YS and UTS of each specimen group (on the right)

ASTM A36 steel, which has nearly identical chemical composition regarding ER70S-6 [34].

Figure 12 presents three engineering stress-strain curves of the tensile specimen v-TS1, h-TS1, and b-TS1, which are representative for three groups of tensile specimens. The strain-stress curves of all specimens present a typical behavior of low-carbon steels [35]. The yield strength (YS offset 0.2%) and the ultimate tensile strength (UTS) of the specimens (h-TSi) in the welding direction (horizontal) are relatively lower than those of the specimens v-TSi in the building direction (vertical), where $i = \{1, 2, \text{and } 3\}$. The average YS and UTS values of the specimens v-TSi are 362 ± 8 MPa and 479 ± 7 MPa respectively, whereas the specimens h-TSi present an average value of 320 ± 6 MPa for the YS and 429 ± 8 MPa for UTS (Fig. 12).

The difference of tensile strengths between the building direction (vertical) and the welding direction (horizontal) is caused by the inhomogeneity in terms of microstructures of the GMAWAM-built feature. The specimens along the

welding direction show a significantly higher elongation at the broken point than that of the specimens along the building direction. This also indicates the prominence of anisotropy in ductility of built materials.

In comparison with the available data published in the literature (Table 2), the tensile strengths (YS and UTS) of the single-bead multi-layer low-carbon steel (ER70S-6) features built by using GMAWAM are relatively lower. In some cases, the YS and UTS values obtained in this study are similar to those observed in [32, 34]. Most of the tensile properties of GMAWAM wall are also lower than those of traditionally as-welded ER70S-6 (UTS = 590 MPa, YS = 470 MPa [26]), except the case presented in [7], where UTS = 618.5 ± 10.8–693.5 ± 8.5 MPa and YS = 461.5 ± 6.3–519.5 ± 8.3 MPa. The YS and UTS values also vary depending on deposition strategies, process parameters, and shielding gasses used to build the walls. In fact, using different deposition strategies, process parameters, and cooling conditions to build the walls causes the thermal cycles and the cooling time that occur in

Table 2 Tensile properties of GMAWAM low-carbon steel (ER70S-6) walls, wrought ASTM A36 steel, and ER70S-6 wire

Strategies for building the walls	Direction	UTS (MPa)	YS 0.2% (MPa)	Elongation (%)	Reference
Single-bead multi-layer deposition	Horizontal	429 ± 8	320 ± 6	-	Current study
	Vertical	479 ± 7	362 ± 8	-	
	Horizontal	≈ 475	≈ 258	-	[34]
	Vertical	≈ 478	≈ 266	-	
	Horizontal	693.5 ± 8.5	519.5 ± 8.3	36.8 ± 0.2	[7]
	Vertical	618.5 ± 10.8	461.5 ± 6.3	28.2 ± 0.5	
Overlapped-bead multi-layer deposition	Horizontal	498 ± 8.8	368 ± 12.2	36 ± 3.5	[32]
	Vertical	501 ± 2.87	368 ± 4.15	32 ± 1.1	
	Horizontal	503 ± 21	402 ± 26	12 ± 3	[21, 36]
	Vertical	490 ± 21	396 ± 26	35 ± 2	
Oscillated-bead multi-layer deposition	Horizontal	478 ± 6.41	354 ± 13.54	38 ± 2.6	[32]
	Vertical	474 ± 0.94	338 ± 4.37	36 ± 2.2	
Wrought ASTM A36	-	400–550	250	20–23	[37]
As-welded ER70S-6 with 100% CO_2	-	590	470	25	[26]

different ways, which results in the variety of the microstructure of the as-built material in terms of grain size, morphologies, and the distribution of microstructure types in different regions. Therefore, the mechanical properties of the walls built with different strategies and processing conditions are varied accordingly, as shown in Table 2. However, in all cases, it is interesting to see that the YS and UTS of GMAWAM ER70S-6 steel walls are normally higher than those of wrought ASTM A36 steel (YS = 250 MPa and UTS = 400–550 MPa [37]), indicating better material properties achieved by using GMAWAM vs. conventional manufacturing processes.

Lastly, it was revealed that all specimens b-TSi were broken in the middle region of the welded material instead of in the interface between the deposited materials and the substrate (Fig. 12a). The average YS and UTS values are similar to those of the vertical specimens (v-TSi) and equal to 355 ± 7 MPa and 468 ± 8 MPa, respectively. This allows us to confirm that the built feature has a strong metallurgical bonding with the substrate, and the new part has a good material quality that meets specification requirements for real applications.

4 Conclusions

In this study, the internal quality of GMAWAM-repurposed components was investigated. The results indicate that GMAWAM-repurposed components show any major defects (e.g., cracks and macro-porosity). The microstructure and mechanical properties of GMAWAM low-carbon steel features are compatible with industrial requirements. The results of the metallurgical and tensile tests confirm that the new features also have strong metallurgical bonding with the existing part. Therefore, it can be considered that the internal quality of repurposed components is adequate for real applications. Moreover, the center of the existing part was not significantly affected by the heat source during the build of new features. Hence, the original properties of the base material were mostly preserved.

Compliance with ethical standards

References

1. Le VT, Paris H, Mandil G (2017) Environmental impact assessment of an innovative strategy based on an additive and subtractive manufacturing combination. J Clean Prod 164:508–523. https://doi.org/10.1016/j.jclepro.2017.06.204
2. Le VT, Paris H (2018) A life cycle assessment-based approach for evaluating the influence of total build height and batch size on the environmental performance of electron beam melting. Int J Adv Manuf Technol 98:275–288. https://doi.org/10.1007/s00170-018-2264-7
3. Huang S, Liu P, Mokasdar A, Hou L (2013) Additive manufacturing and its societal impact: a literature review. Int J Adv Manuf Technol 67:1191–1203. https://doi.org/10.1007/s00170-012-4558-5
4. Guo N, Leu M (2013) Additive manufacturing: technology, applications and research needs. Front Mech Eng 8:215–243. https://doi.org/10.1007/s11465-013-0248-8
5. Frazier WE (2014) Metal additive manufacturing: a review. J Mater Eng Perform 23:1917–1928. https://doi.org/10.1007/s11665-014-0958-z
6. Dutta B, Froes FH (2014) Additive manufacturing of titanium alloys. Adv Mater Process 172:18–23
7. Lu X, Zhou YF, Xing XL, Shao LY, Yang QX, Gao SY (2017) Open-source wire and arc additive manufacturing system: formability, microstructures, and mechanical properties. Int J Adv Manuf Technol 93:2145–2154. https://doi.org/10.1007/s00170-017-0636-z
8. Karunakaran KP, Suryakumar S, Pushpa V, Akula S (2010) Low cost integration of additive and subtractive processes for hybrid layered manufacturing. Robot Comput Integr Manuf 26:490–499. https://doi.org/10.1016/j.rcim.2010.03.008
9. Williams SW, Martina F, Addison AC, Ding J, Pardal G, Colegrove P (2016) Wire + arc additive manufacturing. Mater Sci Technol 32:641–647. https://doi.org/10.1179/1743284715Y.0000000073
10. Cunningham CR, Flynn JM, Shokrani A, Dhokia V, Newman ST (2018) Invited review article: strategies and processes for high quality wire arc additive manufacturing. Addit Manuf 22:672–686. https://doi.org/10.1016/j.addma.2018.06.020
11. Ding D, Pan Z, Cuiuri D, Li H (2015) Wire-feed additive manufacturing of metal components: technologies, developments and future interests. Int J Adv Manuf Technol 81:465–481. https://doi.org/10.1007/s00170-015-7077-3
12. Xiong J, Li Y, Li R, Yin Z (2018) Influences of process parameters on surface roughness of multi-layer single-pass thin-walled parts in GMAW-based additive manufacturing. J Mater Process Technol 252:128–136. https://doi.org/10.1016/j.jmatprotec.2017.09.020
13. Wu B, Pan Z, Ding D, Cuiuri D, Li H, Xu J, Norrish J (2018) A review of the wire arc additive manufacturing of metals: properties, defects and quality improvement. J Manuf Process 35:127–139. https://doi.org/10.1016/j.jmapro.2018.08.001
14. Iványabernero PA, Álvarez P, Suárez A (2018) Study on arc welding processes for high deposition rate additive manufacturing. Procedia CIRP 68:358–362. https://doi.org/10.1016/j.procir.2017.12.095
15. Ortega AG, Corona Galvan L, Salem M, Moussaoui K, Segonds S, Rouquette S, Deschaux-Beaume F (2019) Characterisation of 4043 aluminium alloy deposits obtained by wire and arc additive manufacturing using a cold metal transfer process. Sci Technol Weld Join 24:538–547. https://doi.org/10.1080/13621718.2018.1564986
16. Gomez Ortega A, Corona Galvan L, Deschaux-Beaume F, Mezrag B, Rouquette S (2018) Effect of process parameters on the quality of aluminium alloy Al5Si deposits in wire and arc additive manufacturing using a cold metal transfer process. Sci Technol

Weld Join 23:316–332. https://doi.org/10.1080/13621718.2017.1388995

17. Geng H, Li J, Xiong J, Lin X (2017) Optimisation of interpass temperature and heat input for wire and arc additive manufacturing 5A06 aluminium alloy. Sci Technol Weld Join 22:472–483. https://doi.org/10.1080/13621718.2016.1259031

18. Zhao H, Zhang G, Yin Z, Wu L (2013) Effects of interpass idle time on thermal stresses in multipass multilayer weld-based rapid prototyping. J Manuf Sci Eng 135:011016. https://doi.org/10.1115/1.4023363

19. Suryakumar S, Karunakaran K, Chandrasekhar U, Somashekara M (2013) A study of the mechanical properties of objects built through weld-deposition. Proc Inst Mech Eng Part B J Eng Manuf 227:1138–1147. https://doi.org/10.1177/0954405413482122

20. Liberini M, Astarita A, Campatelli G, Scippa A, Montevecchi F, Venturini G, Durante M, Boccarusso L, Minutolo FMC, Squillace A (2017) Selection of optimal process parameters for wire arc additive manufacturing. Procedia CIRP 62:470–474. https://doi.org/10.1016/j.procir.2016.06.124

21. Rafieazad M, Ghaffari M, Vahedi Nemani A, Nasiri A (2019) Microstructural evolution and mechanical properties of a low-carbon low-alloy steel produced by wire arc additive manufacturing. Int J Adv Manuf Technol 105:2121–2134. https://doi.org/10.1007/s00170-019-04393-8

22. ElMaraghy H, Moussa M (2019) Optimal platform design and process plan for managing variety using hybrid manufacturing. CIRP Ann 68:443–446. https://doi.org/10.1016/j.cirp.2019.03.025

23. Bauer T, Brissaud D, Zwolinski P (2017) Design for high added-value end-of-life strategies:113–128. https://doi.org/10.1007/978-3-319-48514-0_8

24. Le VT, Paris H, Mandil G (2018) The development of a strategy for direct part reuse using additive and subtractive manufacturing technologies. Addit Manuf 22:687–699. https://doi.org/10.1016/j.addma.2018.06.026

25. Le VT, Paris H, Mandil G, Brissaud D (2017) A direct material reuse approach based on additive and subtractive manufacturing technologies for manufacture of parts from existing components. Procedia CIRP 61:229–234. https://doi.org/10.1016/j.procir.2016.11.190

26. The Lincoln Electric Company: MIG (GMAW) WIRE n.d. https://lincolnelectric.com/assets/global/Products/Consumable_MIGGMAWWires-SuperArc-SuperArcG4Si1/c41025.pdf. Accessed 3 Sept 2020

27. Pham TH, Kim JJ, Kim SE (2014) Estimation of microstructural compositions in the weld zone of structural steel using nanoindentation. J Constr Steel Res 99:121–128. https://doi.org/10.1016/j.jcsr.2014.04.011

28. Montevecchi F, Venturini G, Grossi N, Scippa A, Campatelli G (2018) Idle time selection for wire-arc additive manufacturing: a finite element-based technique. Addit Manuf 21:479–486. https://doi.org/10.1016/j.addma.2018.01.007

29. Zhao H, Zhang G, Yin Z, Wu L (2011) A 3D dynamic analysis of thermal behavior during single-pass multi-layer weld-based rapid prototyping. J Mater Process Technol 211:488–495. https://doi.org/10.1016/j.jmatprotec.2010.11.002

30. Yang D, Wang G, Zhang G (2017) Thermal analysis for single-pass multi-layer GMAW based additive manufacturing using infrared thermography. J Mater Process Technol 244:215–224. https://doi.org/10.1016/j.jmatprotec.2017.01.024

31. Shassere B, Nycz A, Noakes MW, Masuo C, Sridharan N (2019) Correlation of microstructure and mechanical properties of metal big area additive manufacturing. Appl Sci 9. https://doi.org/10.3390/app9040787

32. Aldalur E, Veiga F, Suárez A, Bilbao J, Lamikiz A (2020) High deposition wire arc additive manufacturing of mild steel: strategies and heat input effect on microstructure and mechanical properties. J Manuf Process 58:615–626. https://doi.org/10.1016/j.jmapro.2020.08.060

33. Khalid FA, Farooque M, ul Haq A, Khan AQ (1999) Role of ferrite/pearlite banded structure and segregation on mechanical properties of microalloyed hot rolled steel. Mater Sci Technol 15:1209–1215. https://doi.org/10.1179/026708399101505121

34. Haden CV, Zeng G, Carter FM, Ruhl C, Krick BA, Harlow DG (2017) Wire and arc additive manufactured steel: tensile and wear properties. Addit Manuf 16:115–123. https://doi.org/10.1016/j.addma.2017.05.010

35. Yan JB, Liew JYR, Zhang MH, Wang JY (2014) Mechanical properties of normal strength mild steel and high strength steel S690 in low temperature relevant to Arctic environment. Mater Des 61:150–159. https://doi.org/10.1016/j.matdes.2014.04.057

36. Ghaffari M, Vahedi Nemani A, Rafieazad M, Nasiri A (2019) Effect of solidification defects and HAZ softening on the anisotropic mechanical properties of a wire arc additive-manufactured low-carbon low-alloy steel part. Jom 71:4215–4224. https://doi.org/10.1007/s11837-019-03773-5

37. ASTM A36 Steel, plate n.d. http://www.matweb.com/search/DataSheet.aspx?MatGUID=afc003f4fb40465fa3df05129f0e88e6&ckck=1. Accessed 30 Sept 2020